PRL-TN-2023-118

Technical Note

# Design and Development of Dust Detector

by

S. N. Nambiar, J. P. Pabari, S. Jitarwal, Rashmi K. Acharyya, V. Sheel & Anil Bhardwaj

भौतिक अनुसंधान प्रयोगशाला, अहमदाबाद
Physical Research Laboratory, Ahmedabad

*Published by*
*The Dean's office, PRL.*

**PRL Technical Note**
**PRL-TN-2023-118**

# Design and Development of Dust Detector

S. N. Nambiar*, J. P. Pabari, S. Jitarwal, Rashmi, K. Acharyya, V. Sheel & Anil Bhardwaj

*Received 07 December 2022; revised 22 March 2023; accepted 24 March 2023; published 24 March 2023.*

**Abstract**
Interplanetary Dust Particles (IDPs) are nano to micro sized dust grains, found throughout our solar system. They are primarily formed through collisions of asteroids and from cometary debris and they evolve dynamically under various forces including gravity. A dust detector is being developed for future planetary missions to study these interplanetary dust in space. It works on the principle of impact ionization where, plasma generated from impact of particle travelling at hypervelocity on the detector target is collected and processed to derive physical properties of particles. Different design aspects of the detector including mechanical design and electronics is discussed. Further, the detector has to be calibrated using a dust accelerator. In absence of such facility in India, initial testing is carried out using pulse laser facility setup at IPR, Gandhinagar. The tests and equivalence relation between dust and pulse laser is also discussed.

**Keywords**
Interplanetary Dust, Instrumentation, Impact Ionization Detector

[1] *Planetary Sciences Division, Physical Research Laboratory, Ahmedabad*
***S. N. Nambiar**:srirag@prl.res.in

## Contents



## 1. Introduction

### 1.1 Interplanetary Dust

Our solar system is filled with tiny dust grains originating from different sources and is a great source of information for looking into the past. Asteroids in the belt between Mars and Jupiter, on collision generate immense amount of smaller particles. Comets leave out dust and gas when move closer to Sun. Planetary bodies without atmosphere like Earth's Moon generates dust particles when impacted by meteoroids at very high velocity. Moreover, insterstellar dust, coming from outside our solar system, have been detected by various dust detectors at high heliocentric latitude and are nano-sized grains travelling at high velocity (Altobelli et al., 2006). The IDPs evolve dynamically under different forces like: Gravity of the Sun and planetary bodies, solar radiation pressure, Poynting-Robertson (PR) drag, solar wind pressure and Lorentz force. All these forces together along with collision decide the evolution and lifetime of these particles. Figure 1 shows that larger particles (>0.1$\mu$m) spiral in towards Sun due to gravitational attraction whereas smaller grains (beta meteoroids) are blown outwards by radiation pressure (Berg and Grün, 1973). By studying the present distribution, we can understand the evolution and effect of different forces acting on the particles. Further, when these particles enter a planetary atmosphere, they are burnt and leave out metallic

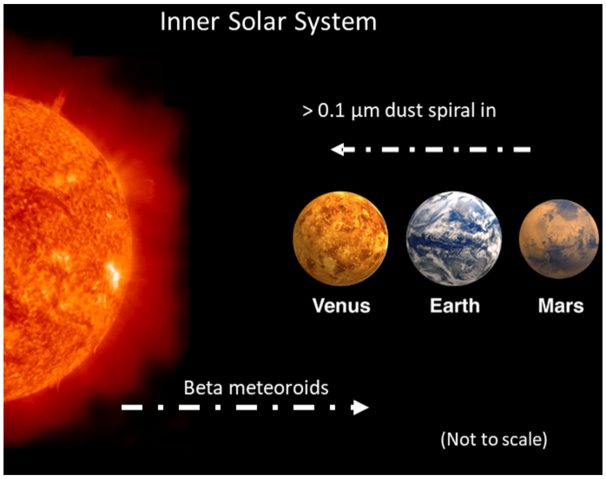


**Figure 1.** Dynamics of dust within solar system due to different forces. Larger particles spiral inwards becasue of gravitational force while smaller particles are blown outwards because of radiation pressure.

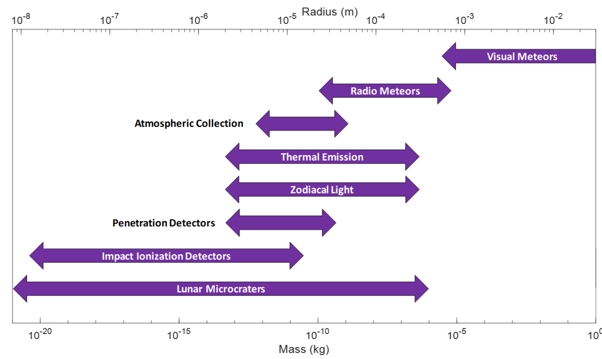


**Figure 2.** Different detection techniques to study IDPs in different mass or size ranges (modified after Sykes et al. (2004)). Larger particles are observed visually or through radio echo from ionizing meteoroids. Atmospheric collections of an IDP's remaining are usually carried out using aeroplanes. Large scale survey of micron sized particles are carried out using zodiacal light or infrared observatoions. To study smaller particles in-situ detectors are used while lunar microcrate study allows analysis of larger range of particle size, however, this requires lunar sample.

ions which results in an additional ionospheric layer and changes in atmospheric chemistry (Carrillo-Sanchez et al., 2020). On impact with airless bodies like Moon, Phobos, Deimos etc., they can cause ejection of regolith and volatile from surface. Dust distribution in a system is closely related to presence of planets and hence dust distribution has been used in discovery of exoplanets as well. Since these particles come from different sources, they hold information regarding their source and helps us infer the prevalent condition under which they were formed or modified. Impact of such high speed particles can cause damage to spacecraft in space and hence understanding such high speed streams is necessary to avoid a catastrophe.

### 1.2 Detection of IDPs and Types of In-Situ Detector

Interplanetary dust have been observed using a variety of instruments, each with its own merits and limitations. Study of light scattered by dust in infrared wavelength can help in understanding the wide scale distribution of particles greater than micrometer size. Figure 2 shows different techniques by which interplanetary dust has been studied along with the particle mass range. Each method is sensitive to different particle mass range and a combined measurement will provide a holistic view of IDPs.

Several in-situ detectors have been flown in past space missions, some of which are discussed below: Acoustic Sensors: Impact of particle at high speed on acoustic sensor gives a output signal based on which particle parameters are estimated. However, here the flux of particles is usually overestimated due to cosmic ray burst and mechanical noises. Capacitor Type: These are penetration detectors where particle have to penetrate the capacitor plate and the insulator. A short along the path of the particle between the two capacitor plates gives a current pulse; the minimum energy or momentum is given by the thickness of the upper capacitor plate. However, smaller particles are not able to penetrate the plate, but plates and insulator must have a certain minimum of thickness because of several noise sources. Film sensor: Polyvinylidene fluoride (PVDF) is a semicrystalline, ferroelectric polymer compound which after processing shows high piezoelectricity and pyroelectricity (Hirai et al., 2014). Film made of permanently polarized PVDF is most commonly used where an impacting particle generates depolarization signal as it penetrates the film. No high bias voltage or extra components are required for such detection and so is a relatively inexpensive technique. Here also, however, only particles greater than micron size can be detected. Student Dust Counter (SDC) on-board New Horizons Mission (Horányi et al., 2008) and ALADDIN on-board IKAROS (Hirai et al., 2014) are two examples of PVDF based detectors. Impact Ionization Detector (IID): An IID works on the following principle: Particle impacts on a metal target and because of the high energy involved, the particle and part of target vaporises and generates plasma. The electrons and ions in this plasma are collected using voltage biased plates. This signal is then processed to derive particle properties like mass, velocity and flux. IID covers larger range particle size as compared to other detectors and can detect particle as small as 100 nm for which the flux is highest. Galileo Dust Detection System (Grün et al., 1992a), Ulysses Dust Detector (Grün et al., 1992b), Cassini Dust Analyser (CDA) (Srama et al., 2004), Mars Dust Counter on-board Nozomi (Igenbergs et al., 1998), LDEX on-board LADEE (Horányi et al., 2014) are some of the examples IID type detectors that were recently flown.

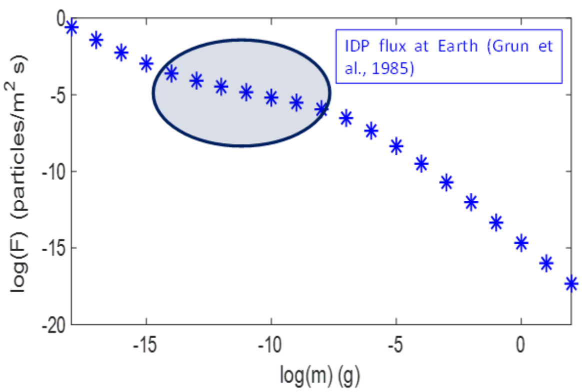


**Figure 3.** Flux at 1 AU (modified after Grün et al. (1985))

The environment of particles and debris near Earth has been studied by multiple instruments in past with different measurement techniques. For example, the Long Duration Exposure Facility (LDEF) on-board ISS was used as a passive detector to study particle impacts in Low Earth Orbit (LEO) (Mandeville, 1991). Typically, such passive surfaces are exposed for long duration in space and the impact craters are analysed using microscopes to measure the features of the impact crater and to derive the flux of particle. Timeband Capture Cell Experiment (TiCCE) on-board European Retrievable Carrier (EuReCa) spacecraft utilised four Al foils and plate to capture the impactor and its evaporated material (Yano et al., 1996).

### 1.3 Interaction with Planetary Bodies

Moon, without an atmospheric layer, gets constantly bombarded with dust particles. Hence, lunar samples also serve as a passive sensor with large exposure times. Grün et al. (1985) made use of such lunar micro-craters and combined it with observation from Pegasus and HEOS-2 satellite to derive a flux model for particles at 1 AU, which is shown in figure 3. As observed, the flux for smaller size particle, which is governed by beta meteoroids is higher as compared to larger particles. This is reinforced by collisional environment of these particles which limit the lifetime of particles greater than $10^{-7}$ kg to $\sim 10^4$ years at 1 AU. The highlighted mass range in the plot shows the detectable mass range of VODEX.

For the case of planets like Earth, Mars and Venus, these particles interact with the atmospheric layer first. Meteor observation using radio telescopes have also been used to get an estimate of flux of meteoroids entering Earth atmosphere and their possible sources. A transverse scatter radar observes specular reflection from meteor train and employs a broad beam whereas, a head echo scatter radar employs a focused beam and observes radiation reflected from head of the meteoroid. Hunt et al. (2004) determined the meteor entry speeds from the high-gain ALTAIR radar. Galligan and Baggaley (2004) made use of Advanced Meteor Orbit Radar (AMOR) to observe more than $10^5$ meteor trains over 5 years and provided meteoroid orbital distribution at 1 AU. AMOR could detect a particle of $10^{-10}$ kg entering at 40 km/s. Campbell-Brown (2008) analysed 5 years of data from Canadian Meteor Orbit Radar (CMOR) and observed presence of a ring structure which is centered on Earth's apex direction with a radius of around 55°. The ring is much weaker as compared to other source of sporadic meteors. CMOR could detect meteoroids of mass $10^{-7}$ kg entering at 30 km/s and larger mass at corresponding lower velocity. Wiegert et al. (2009) developed a dynamic model for sporadic meteoroids observed in Earth's atmosphere, which was calibrated using observation from CMOR. They established that the ring structure is a dynamic phenomenon occurring because of Kozai effect. Though radar observation provides rich data on larger meteroids entering Earth atmosphere, most of the flux of particles which is concentrated at lower mass, is not detected by the radar.

Earth's ionosphere has multiple layers with enhancement in electron and ion density. The D layer between 50 and 90 km is caused by X-ray radiation or specifically the Lyman-alpha radiation ionizing Nitric oxide. The E layer between 90 and 150 km is caused by soft X-ray and far ultraviolet radiation and the F layer at higher altitudes of ~400 km is caused by extreme UV radiation. Over and above the three permanent layers a sporadic E layer, which are thin layers and occur intermittently at altitudes between 90 and 120 km is observed in terrestrial atmosphere (Whalley and Plane, 2010). The source of this layer is ablation of meteors entering Earth atmosphere which leave out metallic ions. A similar transient layer has been reported in Mars's atmosphere between 70 and 110 km and is explained using ablation model (Crismani et al., 2017; Whalley and Plane, 2010; Carrillo-Sánchez et al., 2020). Further, a meteor layer is expected in Venusian atmosphere (Carrillo-Sánchez et al., 2020) which has been observed by (Tripathi et al., 2022) using radio occultation experiment on-board Akatsuki mission.

## 2. Dust Detector Instrument

### 2.1 Principle

We are developing Venus Orbiter Dust Experiment (VODEX), an IID for future Venus mission. On impact at hypervelocity the particle gets completely vaporized and ionized. The ions and electrons in the plasma are separated and collected using voltage biased plates as shown in the figure 4. The charge is converted to voltage signal and by analysing this signal, particle parameters like mass and velocity are derived from equations 1 and 2 (Igenbergs et al., 1998) where $v$ is velocity of the particle and other terms are calibration constants. Further, particle flux is derived from the count rate by determining genuine particle impacts.

The signal rise time is dependent only on the particle velocity as following:

$$t_r = c_g v^{\eta} \tag{1}$$

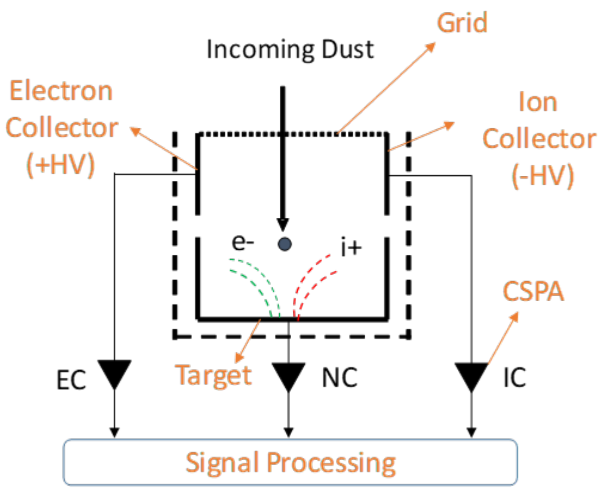


**Figure 4.** Working principle of dust detector (modified after Pabari et al. (2018))

| Parameter | Value |
|---|---|
| Effective Area | 1240 $cm^2$ |
| Particle Velocity Range | 1 km/s to 50 km/s |
| Particle Mass Range (Radius) | $10^{-18}$ to $10^{-12}$ kg<br>(100 nm to 3 μm) |
| Charge Measurement Range* | $5 \times 10^{-15}$ C to $0.5 \times 10^{-12}$ C |
| Dynamic Range | 100 (or 40 dB for voltage) |
| SNR | 6.4 to 46.4 dB |
| Raw Power | 6 W |

**Table 1.** Specifications for Venus Orbiter Dust Experiment (VODEX)

Similarly, the charge to mass ratio is also dependent on particle velocity as following:

$$\frac{Q}{m} = \pm c_r v^{\beta} \tag{2}$$

The dust detector is calibrated using a dust accelerator where particle of known mass and velocity is impacted on the taget. By repeating the experiment for wide range of mass, the calibration curves and constants are derived using equations 1 and 2. Further details on calibration can be found in section 3.

#### 2.1.1 Plasma Expansion

The plasma generated on impact of hypervelocity particle is greatly dependent on the impactor properties. Lee et al. (2013) carried out impact experiments on different target material using Fe particles of $10^{-16}$-$10^{-11}$ g mass range. A Van de Graaff dust accelerator at Max Planck Institute was used to accelerate Fe particles in the velocity range of 1-70 km/s. They utilised multiple sensors including retarding potential analyser (RPA) to measure the impact generated plasma. A theoretical model divided into two parts based on plasma expansion was derived to explain the experimental results. First model describes the early expansion of plasma and the temperature of plasma is derived from it, while the second model is used to relate it to plasma composition and final temperature measured through experiment. In the later expansion of plasma only external electric field is the significant force and initial velocity of species is derived from a half Maxwellian distribution given by

$$f_q(v) = \eta_j Q \sqrt{\frac{2m_j}{\pi k_B T_j}} exp\left(-\frac{m_j v^2}{2k_B T_j}\right) \tag{3}$$

where $v$ is velocity, $\eta_j$ is the fraction, $m_j$ is mass, $T_j$ is temperature of species j, $Q$ is the total charge and $k_B$ is Boltzmann's constant. Based on the comparison between observed results and model, initial temperature of the plasma was found to be 2 eV, which is an order lower than previous estimate.

Fletcher et al. (2015) further worked on simulating plasma from such impacts and confirmed that for large range of impact speeds (30-72 km/s) the plasma temperature remains 2.5 eV. For larger impact speed (30-72 km/s), once the impacting particle is vaporised, bulk of the plasma comes from the target. In this range, the plasma temperature is independant of impactor properties. The plasma gains kinetic energy at the expense of thermal energy and so only the expansion velocity scales with impactor speed. Based on the experimental results, they showed that mass of impacting particle only influences the total amount of charge and crater dimensions, and that it has very little effect on state of charge or plasma temperature. This depends on impact speed. For impact speeds <10 km/s, the plasma temperature was measured to be around 0.5 eV. They observed that plasma transitions from weakly ionized state to fully ionized state at an impact speed of 18 km/s. This transition takes place where $\omega_p/\nu_c = 1$, where $\omega_p$ is plasma frequency and $\nu_c$ is Coulomb collision frequency. Close to the impact site the collision frquency is very high and as the plasma expands, the ratio becomes greater than one. Further, for impact at an angle, the plasma plume was also observed to expand at an angle to target normal, which is different from the pulse laser generated plasma plume. They also verified the empirical equation for crater depth from Drolshagen (2008)

$$d_c = Cm^{0.352}\rho^{0.167}(v * cos\theta)^{0.667} \tag{4}$$

Here, $d_c$ is crater depth in cm, $C$ is a constant dependent on target material, $m, v, \rho, \theta$ are particle mass (g), speed (km/s), density (g/$cm^3$) and impact angle (degree).

### 2.2 Instrument Specifications

Table 1 shows the specification for the dust detector instrument. The effective area of the detector is 1240 $cm^2$ which leads to an overall dimension of 276x254x200 $mm^3$. A particle mass of $10^{-18}$ to $10^{-12}$ kg (100 nm to 3 $\mu$m) and velocity of 1 km/s to 50 km/s can be detected using the instrument. These mass and velocity ranges correspond to a charge range of $5 \times 10^{-15}$ C to $0.5 \times 10^{-12}$ C. This order of charge range, which is typical to dust detectors, is primarily decided by the charge measurable by further electronics chain. The Signal to Noise Ratio (SNR) is computed assuming input signal in the range of 2.5 mV to 250 mV and noise of 1.2 mV (described further in Appendix A). The instrument sensitivity in terms of charge is 5 fC. The measured quantities are signal rise time, peak voltage and count. Here, the rise time of pulse generated by dust particle impact is in the range of 10-50 $\mu$s and the peak voltage is in the range of 10-1000 mV. A raw power of 6 W is required to power the electronics.

The detector design has been optimized with mass as one of the primary constraints. But at the same time, a smaller detector geometry would mean lower number of particles being encountered in space. Hence, design was optimized to maximize the target area within the available mass of the payload. The detector housing is made of Aluminium 6061 and total mass of the payload is slightly below 3 kg. Table 2 shows the payload mass and particle flux for different target sizes. The instrument will be mounted on spacecraft using four M4 sized fasteners through flanges. There are 5 detector PCBs coated with gold which act as target and collector. The detector has an FOV of 140°. Detector mounting in RAM direction of spacecraft is preferred so that additional velocity of spacecraft can be utilised. Also, the detector should possibly be mounted such that it does not come into direct sunlight to avoid saturation by UV rays.

As explained, the instrument measures only the physical properties of particle. The composition of the particle is not measured. For derivation of particle size from its mass, particle density is required and it is assumed. In general, particles encountered in space have density ranging from 0.01 g/cm$^3$ to 5 g/cm$^3$ (Jyoti et al., 1999). Grün et al. (1985) showed that though 20-30% of the particles are of lower density, majority of the particles have density in the range of 2-3 g/cm$^3$. Hence, an assumption of 2.5 g/cm$^3$ would not lead to a large correction. For example, a typical particle of mass $1 \times 10^{-15}$ kg will have size of 0.816, 0.823 and 0.827 $\mu$m with density assumption of 1, 2 and 3 g/cm$^3$ respectively.

#### 2.2.1 Objectives and Observation Modes

The main objective of the VODEX are

- To study the mass-velocity distribution of incoming dust particles at Venus and obtain the nature of particle (as in whether it is interplantary or interstellar)
- To evaluate dust flux at Venus, Earth and the interplanetary space between them
- To estimate the meteoric ion concentration and study its impact in the Venusian lower ionosphere through modelling.

Additionally, if the orbit passes through a cometary debris, it will be characterized. For this purpose, the measurement is to carried out in the Cruise phase to determine flux in interplanetary space and in the orbital phase around Venus to characterize the distribution of dust present there. This will provide an opportunity to compare dust particle environment around Earth and Venus.

### 2.3 Mechanical Aspects

There are three grids present on top of the detector. The lower most grid is grounded and is used to encapsulate the field inside the detector. Solar wind majorly consists of protons, alpha and electrons. The electrons have an energy of 6-17 eV depending on the solar wind condition. The second grid is provided a bias of -100V to deflect these low energy electrons, which helps in noise reduction (Pabari et al., 2022). The third grid is connected to the spacecraft body in order to shield the instrument from external electric fields and to contain the internal electrostatic field. Figure 5 shows mechanical design of VODEX with grids placed at entrance of detection space. The electronics box containing electronics card and power card, stacked one above another, is placed below the detection space. The figure 6 shows an exploded view of the detector.

When a dust particle impacts the metal target of detector, shock waves run into both the impacting particle and target metal. The internal energy produced by the shock is converted into expansion energy and further evaporation and ionization of material (Drapatz and Michel, 1974). The charge from this ionized plasma is collected by the biased plates of detector. Dietzel et al. (1972) showed that maximum conversion of the particle kinetic energy to internal energy of particle available for heating happens when $B_p \rho_p << B_t \rho_t$, where $B$ is shock parameter (empirically derived) $\rho$ is density of material with appropriate subscript for particle and target. This implies that the target should be a material with high density and low deformity. The $B\rho$ value is found to be more for metals as compared to non-metals. Among the metals, this value for gold, which has higher density, is higher. Further, Grün (1984) experimentally showed that the ionization yield on hypervelocity impact of particle on gold and aluminium targets was 4.7 and 0.47 respectively. Hence, traditionally gold is used as target for impact ionization detectors.

For VODEX, the target is made of gold coated PCB. The PCB is used for ease of electrical connection between collecting plate and electronics. The gold coating is done over a copper layer of ~70 $\mu$m. The thickness of gold coating will depend on the crater depth created by an impacting particle. This depth depends on target material properties, incoming particle's mass, speed and density. This relation is given by Frost (1970) as

$$P_d = K m^{0.352} \rho_p^{\frac{1}{6}} v^{\frac{2}{3}} \tag{5}$$

where $P_d$ is penetration depth inside target material, $m$ is mass of the incoming particle in gram, $\rho_p$ is density of particle, $v$ is speed of particle in km/s and $K$ is constant which depends on density of target material as $\rho_t^{-0.5}$. This relation is same as equation 4, only difference being non-consideration of impact

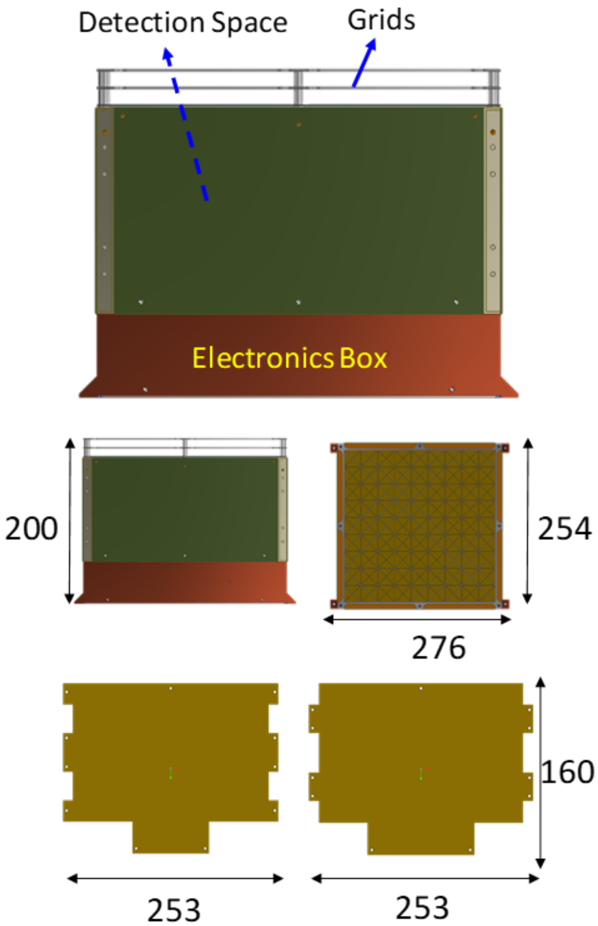


**Figure 5.** Mechanical Design of VODEX with overall dimensions and dimensions of detector PCBs. All dimensions are in mm.

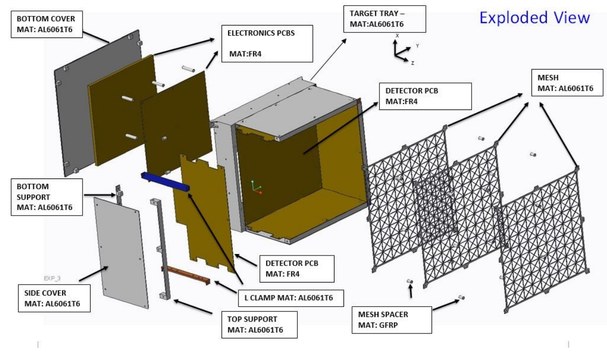


**Figure 6.** Exploded view of Dust Detector

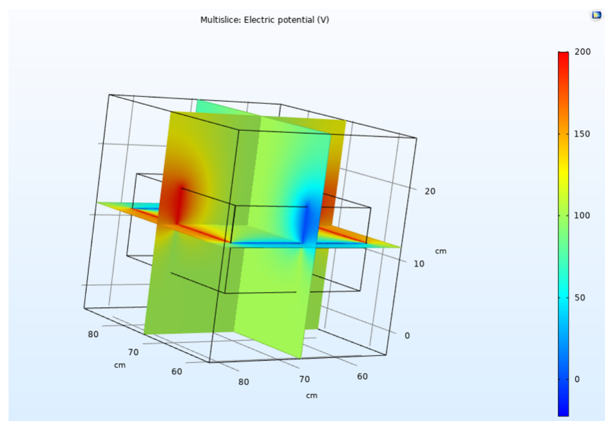


**Figure 7.** Electric potential slice plot for the detector geometry modelled in COMSOL software

angle. From computation we can observe that a particle of $10^{-7}$ g, which is the largest particle expected by the detector during a typical mission lifetime of 5 years, can penetrate upto 60 $\mu$m. Further, due to lower flux, the probability of a particle hitting at a location on target where previous hit has happened is of the order of $10^{-13}$. Hence, the combination of gold and copper should be easily able to protect against any damage by impact.

Table 2 shows the flux of particles that is expected near 1 AU for detectors with different target dimensions. As expected, larger the detector size larger is the flux owing to larger collection area. However, on the downside, larger detector size also implies larger mass of the detector, which are limited resource for any space mission. Also, larger voltage bias will be required to collect the charges for detector with larger dimension, which means more overheads. Hence, a trade off has to be made between particle flux that will be detected and the mass of the detector. With the dimension of $23 \times 23$, we expect a flux of more than 8 particles per day.

The geometry of the detector also defines the detector capacitance, which is an important parameter in detection of small charges. The detector geometry was modelled using COMSOL multiphysics software to derive the capacitance. Figure 7 shows the electric potential slice plot for the detector geometry using which a capacitance of 28 pF was derived. To confirm the same, the capacitance was measured using LCR meter which gave a value of 32 pF, close to modelled value.

To reduce the total mass of payload different material for structure is also being explored. Nomex is a flame-resistant meta-aramid material with honeycomb structure used as core material for sandwich structured composite. It is used for its light weight, larger strength and durability in extreme temperature and radiation environment. Mars Dust Counter utilised a structure made of aluminum and nomex honeycomb (Igenbergs et al., 1998). Figure 8 shows a typical honecomb shaped Nomex sheet and a composite structure made using Nomex and copper coated PCB at ATIRA, Ahmedabad. Figure 8(c) shows detector that was fabricated in-house by bonding commercial nomex composite with copper coated PCB as face on one side. Ten different pieces were bonded using Araldite 2013 to assemble the detector. We are exploring the

| Detector Target Dimension ($cm^3$) | Effective Area ($cm^2$) | FOV (deg) | Cumulative Flux (#/day) | Detector Mass (kg) |
|---|---|---|---|---|
| 15 x 15 | 528 | 120 | 3.61 | 2 |
| 20 x 20 | 794 | 133 | 6.41 | 2.25 |
| 23 x 23 | 977 | 139 | 8.41 | 2.5 |
| 25 x 25 | 1094 | 142 | 9.72 | 3 |

**Table 2.** Flux expected near 1 AU for detector of different dimensions and their respective mass

use of a sandwich material using Nomex and aluminum for the structure of VODEX.

### 2.4 Electronics Architecture

The figure 9 below shows the overall architecture of VODEX. The charge which is generated on impact of particle is in the order of femto to pico Coulomb. Since, this is very small, the signal is converted to voltage and amplified using Charge Sensitive Pre-Amplifier (CSPA). This provides necessary gain to the signal, which is then passed through a buffer for impedance matching. One particular channel i.e. ion channel or electron channel has two collecting PCBs and hence these two signals are added. There is a third channel, connected to the target PCB, which provides indication of start of impact process. Signals from all three channels are digitized using Analog to Digital Converter (ADC). The digital signal is then processed using FPGA to search for impact signal and valid data is stored in the memory, which is then transferred to Satellite subsystem. The voltage required for bias and supply for devices are generated using DC-DC converters.

There are two configurations corresponding to the two channels viz. ion channel and electron channel. For ion channel, which captures the ions the signal would be positive. CSPA inverts this signal and makes it negative. Since, the ADC takes only positive voltage as input, this signal has to be inverted again. For this purpose, the buffer is configured to invert the signal. For electron channel, the incoming signal itself is negative which is made positive by the CSPA. Hence, it can be directly fed into the ADC and so the buffer is used in non-inverting configuration. The detector is configured such that two opposite plates are provided positive bias voltage to collect electrons and the other two plates are negatively biased to collect ions. The signals from two non-inverting buffer is added using a adder as shown is figure 9. The same path is followed for output from two inverting buffer in ion channel. The third channel i.e. neutral channel is connected to the target and is grounded. It will help in determining time of particle impact and will help in identifying genuine dust impacts from noise events. Further, based on the time difference between signals of neutral channel and ion-electron channels, an additional estimation of particle velocity can be made. The architecture of neutral channel is similar to the ion

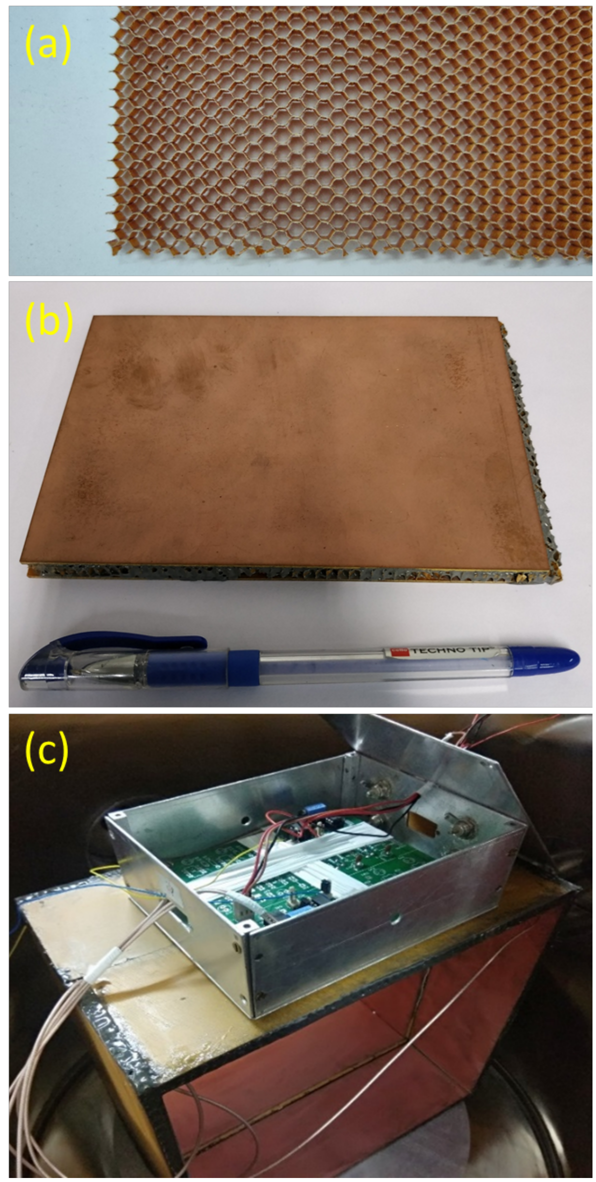


**Figure 8.** (a) Honeycomb shaped Nomex sheet (b) Composite structure fabricated using Nomex as core and Copper coated PCB as face (c) Detector fabricated using commercial Nomex

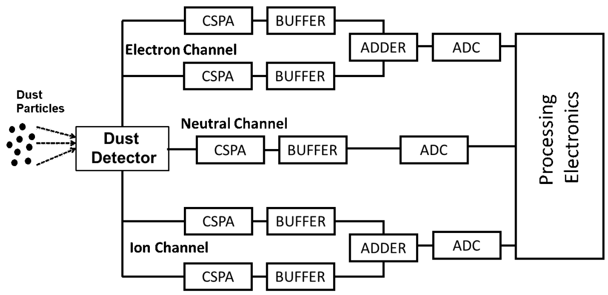


**Figure 9.** Electronics schema of VODEX

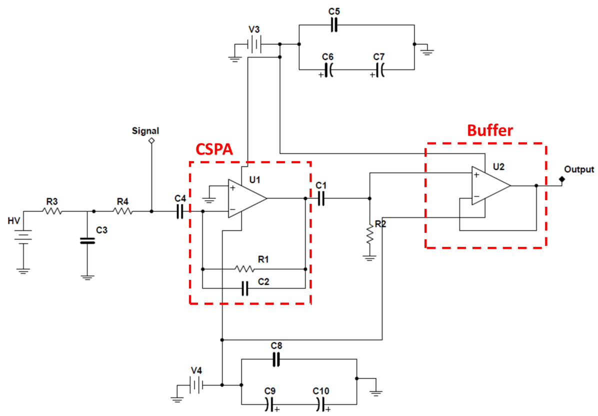


**Figure 10.** CSPA and Buffer configuration

channel without the adder.

The first component in electronics chain, CSPA, basically integrates the current signal and generates voltage signal corresponding to the input charge. The charge is converted to voltage using the feedback capacitor as shown in the figure 10. A value of 0.25 pF is used for this capacitor in our design. The detectable charge range for the detector is 5 fC to 0.125 pC, which roughly corresponds to a particle of 100 nm travelling at 50 km/s and 5 $\mu$m at 5 km/s respectively. The output of CSPA is characterised by a fast rise-time followed by tail pulse. The rise-time depends on velocity of the particle whereas the fall time is governed by the combination of feedback resistor and capacitor. The amplitude of the signal gives information about mass of the particle after velocity is known using equations 1 and 2.

Figure 11 shows detailed block diagram of processing electronics of VODEX. The processing electronics includes Field Programmable Gate Array (FPGA), Analog to Digital Convertor (ADC), Digital to Analog Convertor (DAC) and Crystal Oscillator. To provide the clock signal to the FPGA, a crystal oscillator of 80MHz is used. Using this clock as base, multiple clocks are generated through FPGA for ADC, FPGA's internal RAM, DAC and for data handling. A 49 bit timer is used to time tag the dust impact events. To digitize the incoming signals from electron, ion and neutral channel,

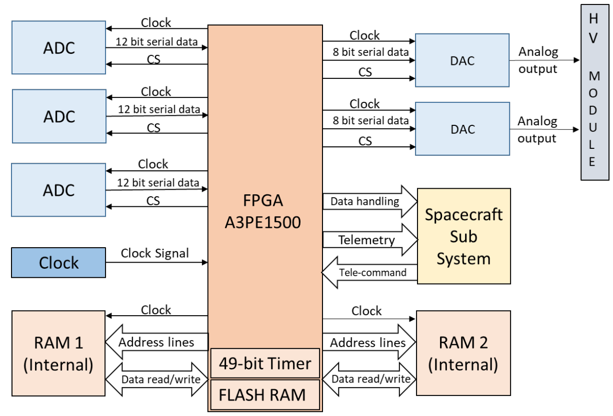


**Figure 11.** Processing electronics of VODEX

three ADCs are used which are operated at sampling rate of 2.5 MSPS. All ADCs provide 10 bit data to FPGA. Since sampling is done at high rate, the data volumes increases to very high value which is difficult to downlink from spacecraft. To reduce the data rate, data is processed such that the signals above a certain threshold level are saved to the FPGA's internal SRAM and is further used for the processing. Once the data is processed, data frames are formed by including header, data and footer in appropriate sequence. Further, to provide the positive and negative high voltage biases to collector plates, high voltage DC-DCs are used. Two DACs are used to provide the reference voltage to DC-DCs and control their output voltage.

As mentioned, high sampling rate leads to high data rate for the instrument. Table 3 shows the expected data rate for VODEX. The computation has been carried out for a worst case of 10000 particles per day and continuous sampling. Data includes 12 bit output of all the three channels sampled at 2.5 MSPS. A window of 300 µs will be saved on detection of dust impact along with a data frame number. The data is time tagged using 32 bits. Health parameters which will be monitored every 30 minutes are also saved. This leads to a data rate of ~3.3 kbps or a data storage requirement of ~280 Mb per day.

## 2.5 Simulations

### 2.5.1 SIMION simulations

Voltage bias is applied to the collector plates, on top of the detector, in order to collect the impact generated electrons and ions. Larger voltage bias will lead suppression of similar charges while very small bias will lead to lower collection efficiency. Further, generating larger bias voltage in space would mean larger risk in case of a short or malfunction. Since, the efficiency of collection is dependent on the voltage bias applied, it is important to optimize the bias. For this purpose, simulations were carried out using SIMION software. SIMION has been used to simulate trajectory of ions and electrons in impact plasma and to compute capture efficiency.

| Quantity | Bits/s |
|---|---|
| Data | 3240 |
| Time Tag | 4 |
| Health Parameter | 1 |
| Data Frame Number | 1 |
| **Total** | **3246** |

**Table 3.** Expected data rate for VODEX

For e.g. Grün et al. (2002) used it to simulate capture efficiency for impact of particle on different parts of cosmic dust analyser. Austin et al. (2002) made use of SIMION to simulate and optimize the time of flight reflectron type spectrometer for Dustbuster instrument.

In SIMION, the detector geometry is first defined and appropriate bias voltage is applied. Then electrons and ions are initiated from an impact point near the target. The initial temperature or kinetic energy of plasma (ions and electrons) is one of the input parameter for simulation. Lee et al. (2013) showed that initial temperature of plasma on impact of particle on metal target is of the order of ~1 eV based on impact experiment and modelling. As these charges evolve in the static electric field, they are captured by the collector plates and collection efficiency is computed. The collection efficiency also depends on the place where impact is considered, depending on the closeness to any of the biased plates. Hence, the simulation was carried out for bias voltages between 50 V and 600 V in steps of 50 V and 100 equally spaced impact positions for each voltage. Figure 12 shows the detector geometry and a typical trajectory of ions and electrons under static electric field. The trajectory for electrons and ions shown are as seen from two adjacent sides of the detector, as two opposite plates have same bias voltage. As the middle grid is negatively biased, some of the ions reach the grid.

Further, simulation was carried out to compare a different bias configuration as well, where two adjacent plates are positively biased and the other two are negatively biased. Then the charge collection efficiency was compared for several impact position on the target with current configuration. For this geometry, the efficiency for impact near biased plate is very low whereas a respectable amount of charge is collected for impact points which is equidistant from both collecting plates. Overall, when compared on the basis of the area of target with sufficient charge collection efficiency, this configuration performs poorly.

As shown in figure 13, the collection efficiency of ions and electrons (red curve) increases with voltage bias but flattens after ~200 V. The collection efficiency also depends on the

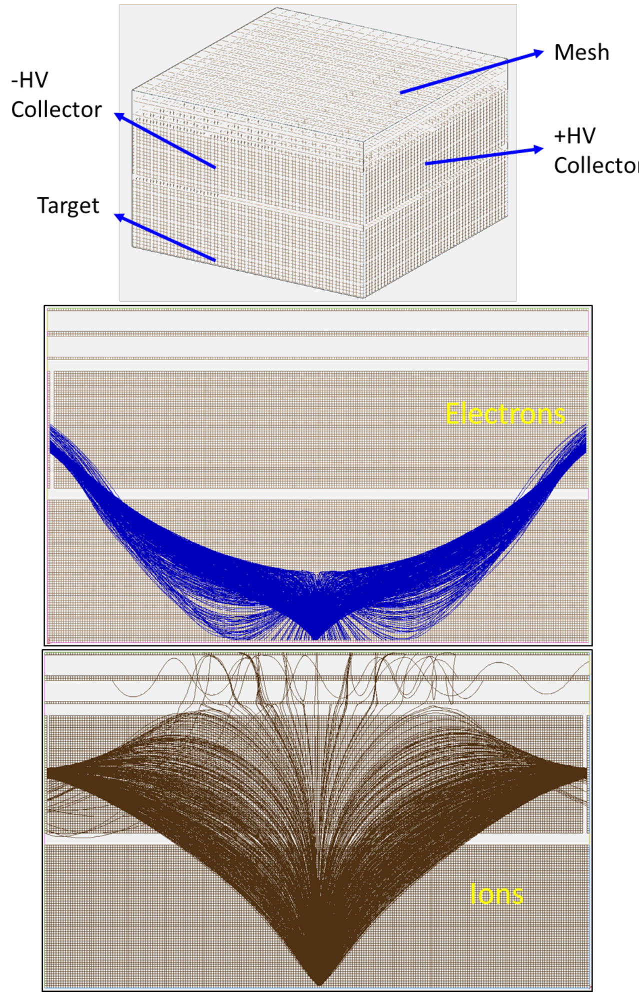


**Figure 12.** SIMION Simulations: Top Pane: The detector geometry defined in SIMION software with appropriate bias. Middle Pane: The trajectory for ions under static electric field for a typical HV bias. Bottom Pane: The trajectory of electrons under same condition

position of impact on target. For example, an impact close to negatively biased collector will cause all ions to be captured and electrons to be repelled or suppressed back to target plate. In presence of electric field electrons follow the field while ions being much heavier are also influenced by their initial velocity. At impact locations where charges are suppressed (near positively biased collector for ions and near negatively biased collector for electrons) following cases occur:

- At lower bias voltages, more number of ions are captured as compared to electrons as electrons follow the field and are mostly suppressed.
- At higher bias voltages, collection of both become close to zero as stronger field suppresses both ions and electrons.

Hence, collection efficiency of ions is more than that of

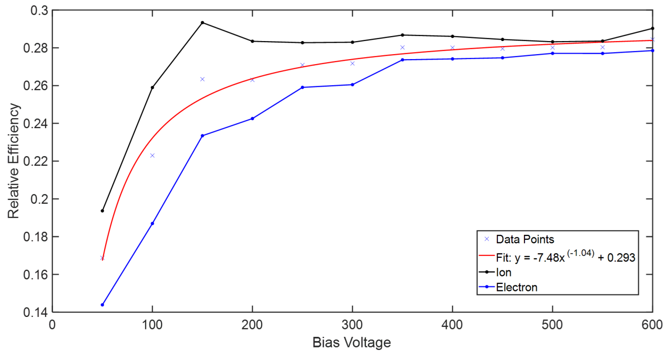


**Figure 13.** Collection efficiency of detector with voltage bias applied to collector plates derived from SIMION simulations. The black and green line shows the collection efficiency for ions and electrons combined with area of target with charge collection greater than 75%. See text for further details.

electrons. This is evident from the black and green lines in figure 13, which shows relative capture efficiency of ions and electrons respectively. The plot is generated by combining the proportion of target area with collection efficiency more than 75% and the actual capture efficiency values at these locations. Two important factors to be considered are: (i) The bias voltage should be enough to capture the ions and electrons and (ii) The bias voltage should not be very large that it repels all of similar charge in case of impact close to a collector and also so that it does increase the resource required owing to higher voltage generation. Based on these arguments, a bias voltage of 200 V is decided for the current detector geometry. Further, refinement is to be done during actual dust impact experiments.

### 2.5.2 GEANT4 simulations

The dust detector is open to space and hence different types of particles and radiation can enter the detector. This may lead to unwanted signals which have to be characterised in order to determine and seperate out genuine particle impacts. The major components that the detector will encounter in space are shown in figure 14. The detector in space will interact with solar wind protons, alpha particle, electrons, Galactic Cosmic Rays (GCR) and radiation belt particles for near Earth orbits. GCR are high energy particles originating outside our solar system and consists of 99% atomic nuclei and 1% electrons, and out of the total atomic nuclei, 90% are proton. The radiation belt electrons are considered for simulation as they are energetic and can pass through the negatively biased second grid on the detector. To study the effect of high energy particles in space on the detector, simulations were carried out using GEANT4 software. Geant4 (for Geometry And Tracking) is a platform for the simulation of the passage of particles through matter using Monte Carlo methods, developed by CERN (Agostinelli et al., 2003). To carry out the simulation, following procedure is followed: (i) The detector geometry

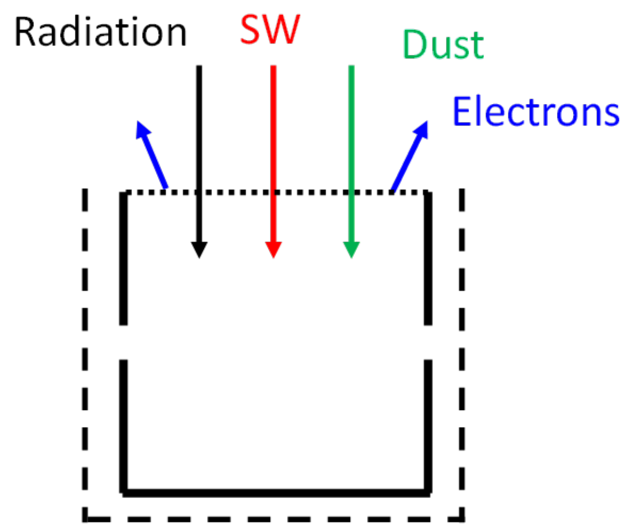


**Figure 14.** Components that the dust detector will encounter in space

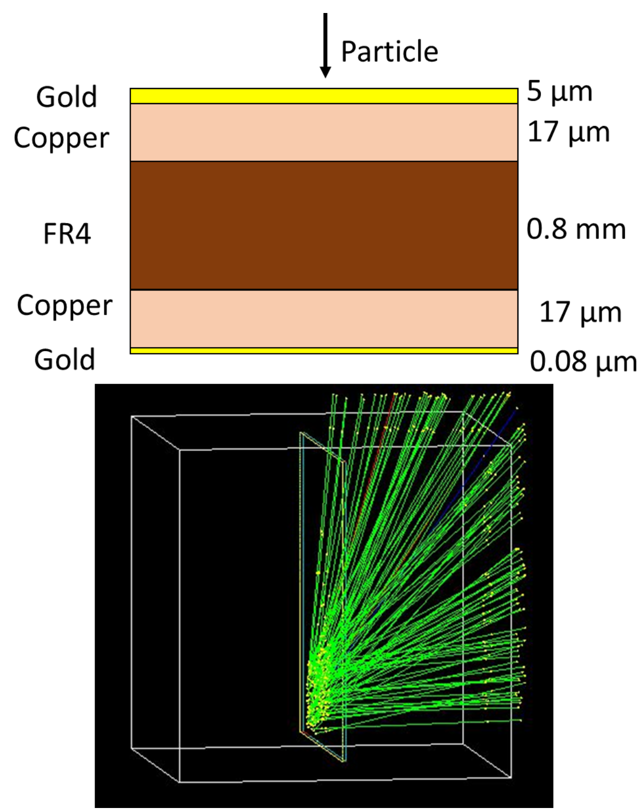


**Figure 15.** Top pane: The structure of target material with thickness of each layer. Bottom pane: A snapshot of simulation run with target material at centre in GEANT4 software. The green lines show trajectory of impacting particles at different angles.

with appropriate material is defined (ii) The impacting particle or radiation with appropriate energy is defined (iii) The particle is allowed to hit and pass through the target material and it loses energy as it interacts with the material (iv) The result is stored and can be visualized (Figure 15).

The results were derived using $10^6$ runs of each particle type. To consider for the angular impact, the angle of incidence was varied between 0° to 90°. The energy ranges were selected from 10 keV to 10 GeV to cover the entire possible range of particles for the proton and alpha particles. The gamma energy varies from 0.5 to 1000 MeV (Ramaty and Mandzhavidze, 1998). The GCR energy is from 10 MeV to 10 GeV. Throughout the energy range, the maximum secondary electrons produced by the solar wind proton, alpha particles, gamma rays, GCR and radiation belt electrons are 9.87%, 36.18%, 4.85%, 9.87% and 15.87% of incoming flux, respectively. Considering that the actual number of secondary electrons produced depend on flux of incoming particle as well, solar wind protons and radiation belt electrons are found to be the major source of secondary electrons. Further, highest number of secondary positron is produced by GCR which is 1.51% of incoming flux. Considering the flux, the effect of positron on ion channel is negligible but effect of secondary electrons on electron channel is considerable. The total secondary electrons generate a noise level of 0.32 fC and 3.77 fC for normal solar condition and an Solar Energetic Particles (SEP) event respectively (Pabari et. al. 2022). The detector has a sensitivity level of ~5 fC, which is a little above the worst-case noise level.

#### 2.5.3 Theoretical Estimate of Noise

To detect an impact generated signal, it should be well above the noise level of detector. For a first hand estimate of this level, noise arising from different sources is estimated theoretically. Thermal noise caused by thermal motion of charges in electronic components and shot noise arising because of the discrete nature of electric charge are considered. The thermal noise from FET, feedback resistor and resistor in high voltage bias line and shot noise due to gate leakage current in FET, detector leakage current and charge variation are computed. The major noise contribution is from feedback and HV bias resistors. Summing contributions from all these sources, a total noise of 0.112 mV is observed, which computed at 85°C for 35 kHz bandwidth. This corresponds to an SNR of 26.9 to 66.9 dB for input signal in the range of 2.5 mV to 250 mV corresponding input charge range. The detailed calculation is provided in Appendix A.

### 2.6 Tests

#### 2.6.1 Functional Tests in Laboratory

The detector and its electronics is tested in laboratory by providing a pulse input using Function generator and the output is observed using oscilloscope. Using this exercise, the amplifier gain and linearity is tested as shown in figure 16 and 17. The instrument is tested for input to CSPA in the range of 1 mV to 400 mV which corresponds to input charge of 0.5 fC to 0.2 pC. This input charge range covers the lower sensitivity level for the instrument and shows the operation of instrument at these levels. The test was carried out for both the inverting and non-inverting configuration of buffer mentioned in section 2.4 and results are provided in Appendix B.

#### 2.6.2 End to End System Test

The End to End test was carried out by connecting the detector, analog electronics and processing electronics. The final output is digital data which is observed using the digital channels of a Mixed Signal Oscilloscope (MSO). Figure 18 shows the processing electronics card of dust detector which receives input from front end electronics. An input pulse is provided to detector using a function generator and final data frame generated by FPGA in processing card is observed. Further testing at lower input signal level is ongoing.

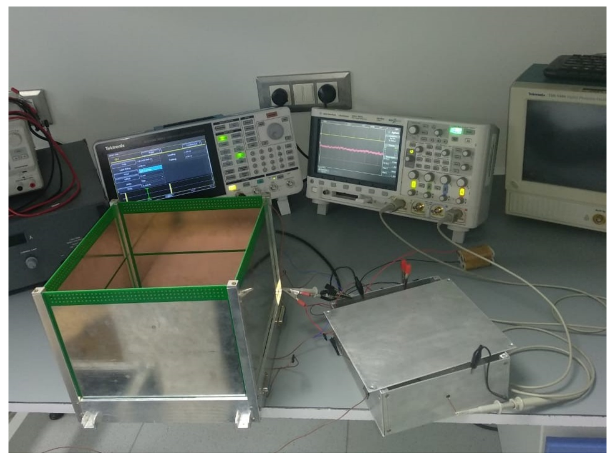

**Figure 16.** Laboratory test setup where detector and electronics is tested using function generator and oscilloscope

#### 2.6.3 Mechanical Tests

The instrument was first tested for random and sine vibration as per the Environment Levels and Test Specifications for PSLV Components and Subassemblies (PSLV/VSS-C/TR/08/83, Issue 5) document for fourth stage of PSLV (PS4). Dummy aluminum plates were used in place of PCB and components. The instrument met the required levels. Later, it was tested as per more harsher Mars Orbiter Mission (MOM) ETLS-ISRO-ISAC-MOM-PR-0997 document. For comparison, the maximum amplitude for sine vibration are 1.4g and 20g for PS4 and MOM respectively. For MOM test level, the fundamental mode was found at 134 Hz as observed in figure 19. The maximum stress at 50g quasi-static loading was 84 MPa, 74 MPa and 113 MPa in X, Y and Z direction respectively, with respective margin of 3.1, 3.7 and 1.4.

Table 4 shows the tests to be carried out to qualify VODEX for space flight. The level of testing will depend on flight requirements. Depending on the performance in each test some rework or change may be needed and appropriate tests have to be repeated.

| Sr No. | Name of the test | Description |
|---|---|---|
| 1 | Initial Bench Test | To check the performance of all the components and verify that it is working within the allowable limits |
| 2 | Thermal Cycling | Passive test to avoid workmanship failure and infant mortality |
| 3 | Burn in test | It is carried out for long time at higher temperature to detect early failure of components |
| 4 | EMI/EMC test | To ensure that proper shielding is present and avoid any electromagnetic interaction with other systems |
| 5 | Sine Vibration test | To determine first mode of resonance frequency and ensure that low frequency vibration during launch environment does not affect the system. |
| 6 | Random Vibration test | To test for workmanship and mission environment |
| 7 | Thermo-vacuum test | To test instrument under space environment |
| 8 | Final Bench Test | To check the performance of all the components post all the tests |

**Table 4.** Above tests are to be carried out in future to qualify the instrument for space flight

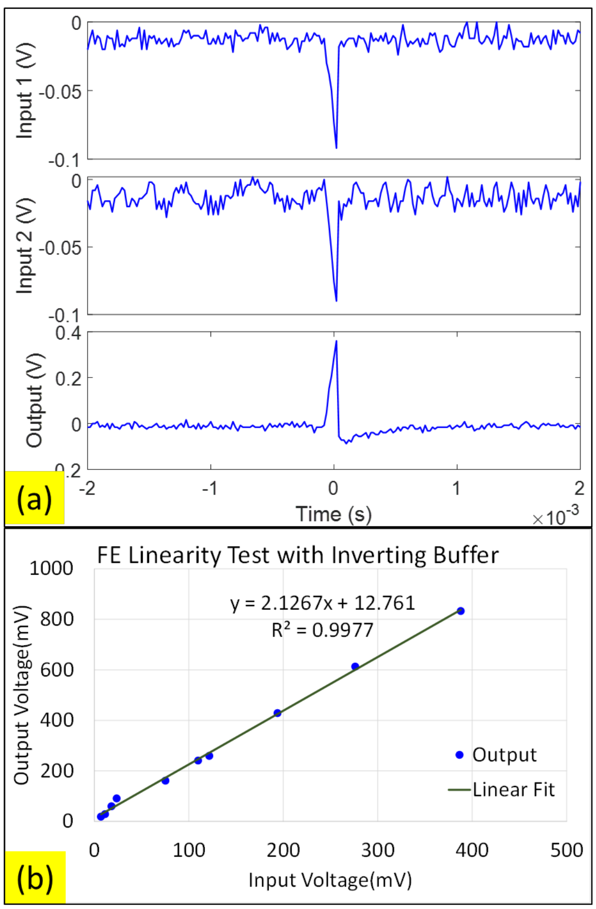


**Figure 17.** Linearity test of Detector + CSPA + Buffer configuration

## 3. Calibration and Instrument Testing at IPR

### 3.1 Calibration Method

The Cosmic Dust Analyser (CDA) on-board Cassini is one of most sophisticated instrument for in-situ dust particle measurement, with two sub-systems: (a) High rate dust detector using PVDF film for determining high impact rates in Saturnian rings and (b) Dust analyser using impact ionization. The dust analyser measures the charge of the particle, impact direction, mass, speed and chemical composition. The chemical composition is measured using a Chemical Analyser Target (CAT) made of rhodium where the particle impacts and generates plasma. The ions are then accelerated towards an electron multiplier and acts as a time of flight (TOF) spectrometer. There are four grids at the entrance of the instrument, with topmost and bottom one being grounded. Amplifier is connected to the two grids in middle and they are inclined at angle of 9°, which aids in determination of particle's direction of arrival. The instrument was mounted on a turntable for better coverage, which could rotate it to an angle of 270°. When a particle encounters CDA, following signals are observed: entrance grid signals, impact ionization target signal, chemical analyser target signal, chemical analyser grid signal, ion collector signal and multiplier signal. Figure 20 shows the configuration of CDA and typical signals on impact of particle on IIT and CAT. All these signals are measured and processed to derive particle's physical parameters and chemical composition (Srama et al., 2004).

Galileo and Ulysses had hemispherical target similar to CDA but did not have a chemical analyser and used only one charge sensing grid. Calibration of Galileo dust sensor is detailed in (Göller and Grün, 1989). On a particle's entry, its charge is first detected by the entrance grid. After the impact of the particle on target the electrons are captured by the target while the ions are captured partly by ion collector grid and remaining by channeltron. The calibration was carried out using dust accelerator facility at Heidelberg which is an electrostatic accelerator. Since, only conducting or

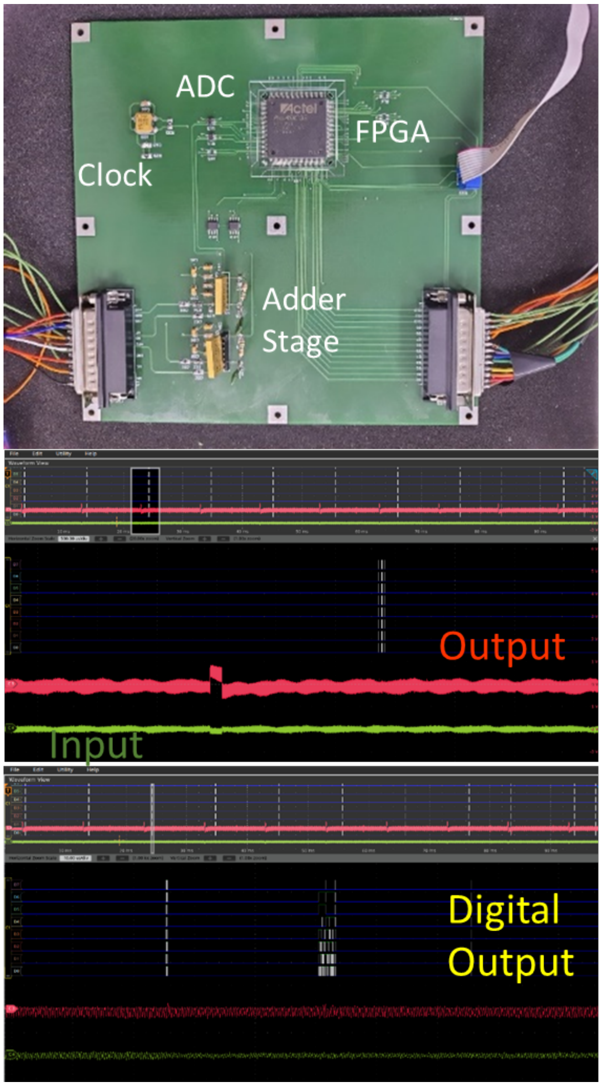


**Figure 18.** Top pane: Processing electronics card of dust detector. Mid pane: The input to detector and output of front end electronics. bottom pane: Data frame generated by FPGA are shown.

metal coated particles could be accelerated, iron, silicate (zinc coated) and carbon particles were used for calibration. The mass and speed range for silicate and carbon particles were lower compared to iron as shown in the figure 21. The calibration was carried out with $10^5$ iron particles and 500 particles of silicate and carbon each. The calibration curve was then derived by averaging all three impact material with equal weights. Further, since the impact angle (angle between target normal and direction of particle's arrival) is not known, tests were carried out at five different impact angles. A calibration curve was then derived by weighting these curves based on the distribution of impact angle. It was observed that for different material and impact angle, the signal rise-time only depended on speed of the particle. Also, the rise-time

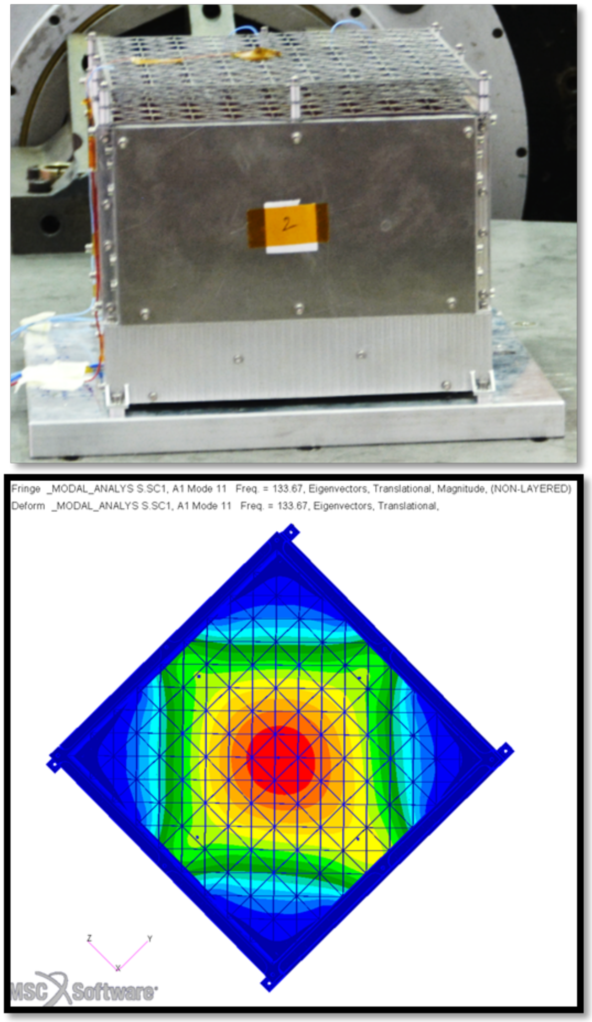


**Figure 19.** Top pane: Dust detector model on vibration shaker. Bottom pane: Vibration analysis result shows the fundamental mode of 134 Hz in Z-direction.

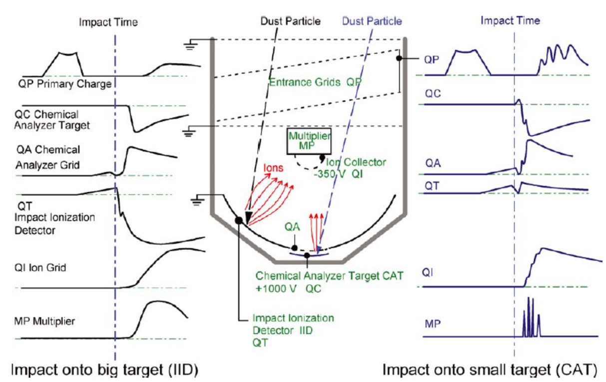


**Figure 20.** Detection principle and signal measurements carried out by Cosmic Dust Analyser which was flown on-board Cassini, taken from Srama et al. (2004)

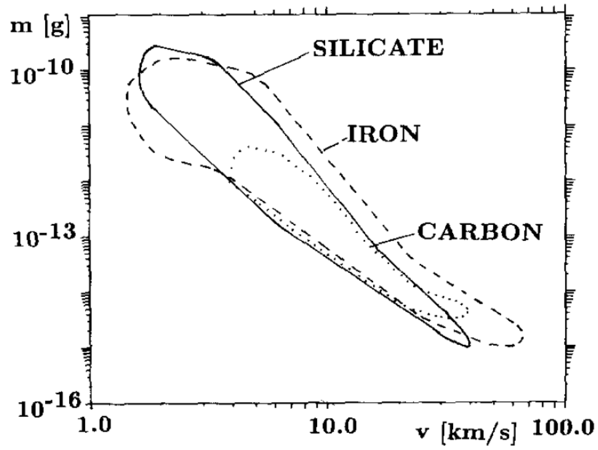


**Figure 21.** Mass and velocity range of particles used for calibration of Galileo dust detector, taken from Göller and Grün (1989)

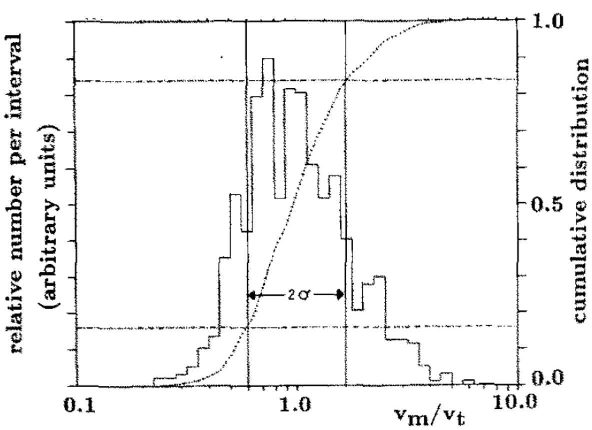


**Figure 22.** The logarithmic distribution of the ratio of measured velocity to true velocity for Galileo dust detector, taken from Göller and Grün (1989)

was found to be a weak function of material and impact angle. The ratio of charge yield to particle mass was also speed dependent. Hence, once the speed and charge yield is known, particle mass could be derived. The time of flight between entrance grid and target impact gives an additional information about speed of the particle. Further, the ratio of charge collected by channeltron to that by ion collector also depended on particle speed and served as an additional check. First, the calibration curves with iron projectile and impact angle of 20° is taken as base. Then two average curves are derived based on different materials and different impact angles. By comparing these average curves to the base curve two correction functions are derived describing the angular ($f_A$) and material variation ($f_M$). Final calibration curve is derived by applying these correction function to the base curve. The accuracy of calibration curve was determined by comparing the measured mass ($m_m$) and speed ($v_m$) using calibration equation with true values ($m_t$, $v_t$) which are measured by particle selection unit of accelerator. Figure 22 shows that histogram of $v_m/v_t$ represents a logarithmic Gaussian curve and hence the deviations are expressed as factors instead of absolute values. The average angle calibration curve for iron projectile was used and the deviation ($\sigma_A$) was calculated in similar way. Then the same process was repeated for average material curve and $\sigma_M$ was computed. Both these deviations also include the inherent error in measurement. Since we are dealing with logarithmic Gaussian distribution function, the error for $log(v)$ is given by $\delta v = log(\sigma_v)$. Using Gaussian error propagation laws we derive the following. Assuming $v_{m0}$ as measured speed for base condition using function $f_0(x)$,

$$v_{m0} = f_0(x) \tag{6}$$

Applying correction function for material and angle variation,

$$\begin{aligned} v_{mA} &= f_0(x) \times f_A(x) = g'_A(x) \\ v_{mM} &= f_0(x) \times f_M(x) = g'_M(x) \end{aligned} \tag{7}$$

Errors $f_0(x)$, $g'_A(x)$ and $g'_M(x)$ are measured using histogram similar to figure 21 ($\sigma_0, \sigma'_A, \sigma'_M$). Using these values error in $f_A$ and $f_M$ are computed using

$$\begin{aligned} \delta_M^2 &= \delta_M'^2 - \delta_0^2 \\ \delta_A^2 &= \delta_A'^2 - \delta_0^2 \end{aligned} \tag{8}$$

The measured speed is obtained by incorporating correction to base function

$$v_m = f_0(x) \times f_A(x) \times f_M(x) \tag{9}$$

which gives a total error of

$$\begin{aligned} \delta &= \sqrt{\delta_0^2 + \delta_M^2 + \delta_A^2} \\ \sigma &= 10^{\delta} \end{aligned} \tag{10}$$

This is the total deviation in determining the speed of the particle of unknown material and impact angle. A similar computation is employed to determine error in measured mass of the particle. Since, derivation of mass utilises measured speed, the error for mass is higher as the error in speed is propagated. Since, VODEX also does not determine composition of the incoming particle, a very similar approach has to be carried out for calibration of the instrument. Since dust accelerator facilities are very few in the world and none available in India, one of the inexpensive way to test the detector is using nanosecond pulse laser.

Since we have to visit a dust accelerator facility situated abroad, we would like to optimize the test plan so that we can characterize the instrument as well as possible with the available limited particle impacts. Table 5 shows the different particle types that we plan to test in the initial phase. It includes

| Radius | Approx. Mass (kg) | Velocity (km/s) | Material |
|---|---|---|---|
| 50 nm | 4E-18 | 20 | Fe |
| 100 nm | 3E-17 | 25 | Fe |
| 100 nm | 3E-17 | 20 | Fe |
| 100 nm | 3E-17 | 20 | $SiO_2$ |
| 100 nm | 3E-17 | 10 | Fe |
| 100 nm | 3E-17 | 5 | Fe |
| 500 nm | 4E-15 | 3 | Fe |
| 3 µm | 9E-13 | 1.5 | Fe |
| 5 µm | 4E-12 | 0.5 | Fe |

**Table 5.** Particle properties to be utilised for initial testing of detector using a dust accelerator facility

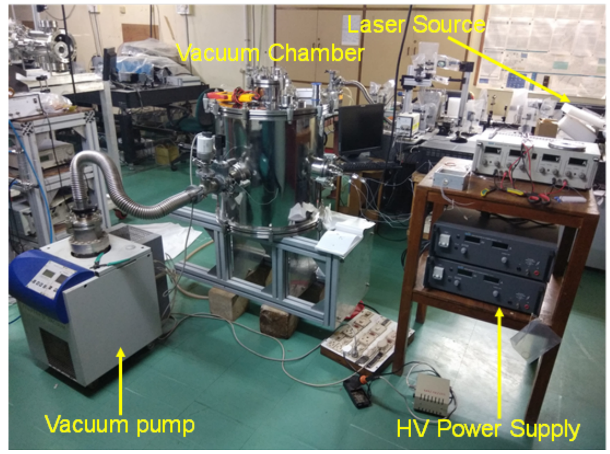


**Figure 23.** Nanosecond pulse laser test setup at IPR Gandhinagar

combination of small and large particles with high and low speeds. The aim is to achieve following objectives: (a) Check the detector output at lower sensitivity level and saturation level. (b) To test detector within its working mass-velocity range. (c) Derive crude calibration equation. (d) Observe the difference in output for different material of particle. (e) Study damage to target PCB due to particle impacts and maybe characterise crater dimensions.

### 3.2 Testing with Pulse laser

A nanosecond pulse laser has been traditionally used to simulate dust particle impact for dust detectors in past missions like Cassini dust detector, ALADDIN etc. The signal derived from a dust impact and pulse laser shot show similar characteristics, primarily the signal risetime, based on which particle parameters are determined. Though the physical process which generates charge is different in pulse laser and dust impact, but the time scale of crater production and energy dissipation of laser is similar. Because of these reasons a nanosecond pulse laser can be reliably used for characterising the electronics. The figure 23 shows the testing setup at IPR Gandhinagar, where detector is placed inside the vacuum chamber. A turbomolecular pump is used to reach the required vacuum level. Q-smart 850 Nd:YAG laser with pulse duration of ~6 ns and wavelength of 532 nm is utilised. The optical setup is shown in figure 24 where the laser beam is diverted to the chamber using mirror. The energy of the laser pulse is controlled using combination of wave plate and beam splitter. The beam is then focused on the target plate of the detector inside chamber using focusing lens. The experiment is conducted at $10^{-4}$-$10^{-5}$ mbar. Figure 25 shows a typical output from pulse laser where, outputs from both electron channel (positively biased) and ion channel (negatively biased) are shown. The amplitude gives an indication of how much charge is collected.

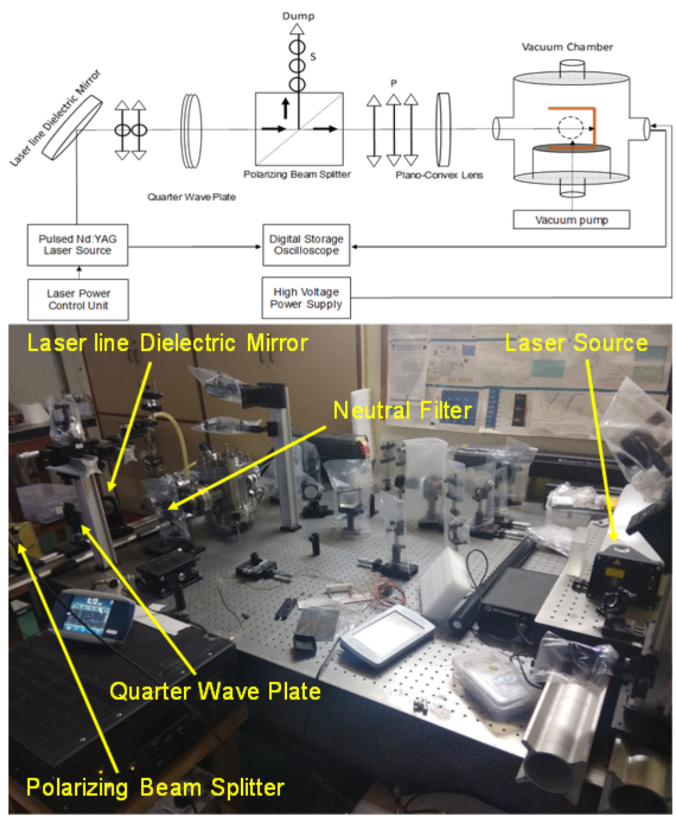


**Figure 24.** Diagram showing optical setup at IPR. The laser beam is passed through polariser and beam splitter and eventually focused using lens on the detector lying inside the vacuum chamber.

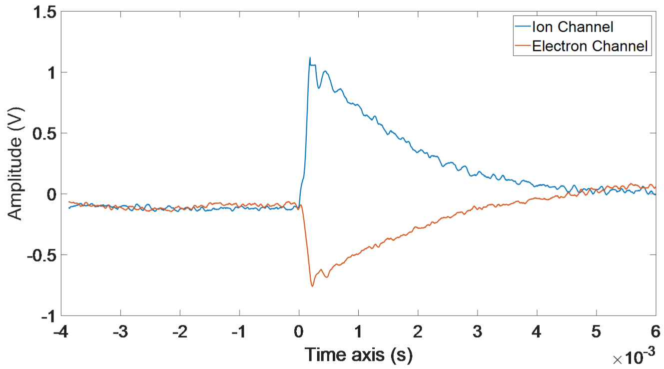


**Figure 25.** A typical output from pulse laser test of dust detetctor

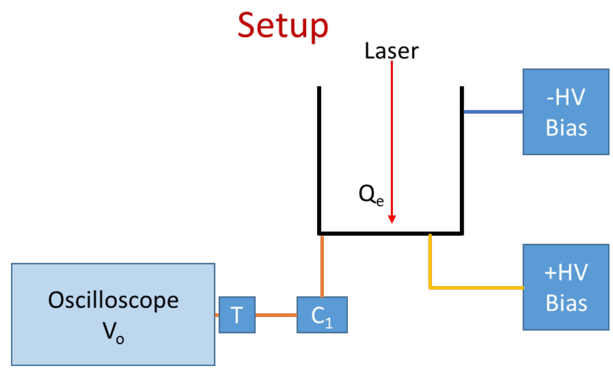


**Figure 26.** Test setup at IPR to derive the equivalence relation

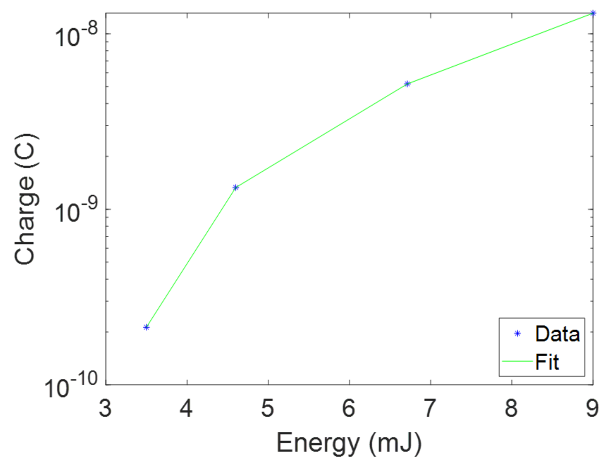


**Figure 27.** Charge generated during pulse laser experiment with different laser energy and a cubic fit to the data.

### 3.3 Equivalence between laser and dust particle

The pulse laser experiment was extended to possibly derive an equivalence between pulse laser shot and particle parameters like mass and velocity. For this, the fraction of laser energy used for ionization is compared to the fraction of kinetic energy of dust that is utilized for ionization. The following equations 11-15 show how the laser and dust are related where, $E_{ip}$ – Particle ionization energy, $E_{iL}$ – Laser ionization energy, $\alpha$– Laser ionization efficiency, $E_L$ – Laser energy, $KE_p$ - Kinetic energy of particle, $v_p$ – Velocity of particle, $m_p$ - Mass of particle and $\beta$ is a constant.

$$\frac{E_{ip}}{KE_p} = 3\times 10^{-6} v_p^{1.7} \tag{11}$$

$$E_{iL} = \alpha \times E_L \tag{12}$$

$$E_{ip} = E_{iL} \tag{13}$$

$$3\times 10^{-6} v_p^{1.7} KE_p = \alpha \times E_L \tag{14}$$

$$E_L = \beta \times v_p^{3.7} m_p \tag{15}$$

First, we compute the laser ionization efficiency by applying high positive bias to target which will collect all the electrons ($Q_e$), generated from ablation. Assuming charge neutrality (i.e. $Q_e = Q_i = Q$) and Qe as the total charge produced by laser, the energy used for ionization is computed using ionization energy per atom of target material. For eg. Ionization energy for gold atom is $1.478\times 10^{-18}$ J, multiplying this with total number of ions (or electrons) generated gives total energy utilized for ionization $E_{iL} = \alpha \times E_L$. This is calculated using the relation $Q = n\times e$ and $E_{iL} = n\times I_T$. Here,$n$ is number of electrons generated and $I_T$ is ionization energy of target material. The setup for this experiment is shown in figure 26.

In the setup $C_1$ = 47 nF and T is termination (50 or 1 M ohm). From the output voltage $V_0$ we derive $Q_e$ using $C_1$. Using this relation we derive the following equivalence relation:

$$E_L = 9.41\times 10^5 \times m_p v_p^{3.7} \tag{16}$$

This relation can be further refined by conducting the experiment at different laser energies especially at lower energies where the laser would closely simulate dust particle in the measurable range of detector.

Pulse laser experiments were conudcted at multiple laser energies to check the variation in charge and equivalence relation. Figure 27 shows charge generated by pulse laser at different laser energies which shows a very good fit with cubic polynomial. This non-linear variation suggests that the constant $\beta$ in equation 15 varies with laser energy. Further

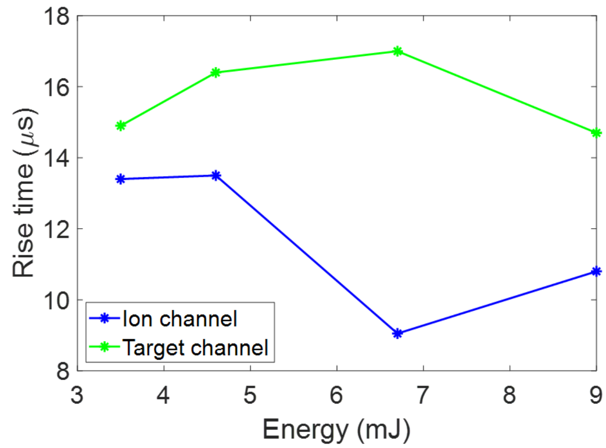


**Figure 28.** Signal rise time for ion channel and target channel. Read text for further description.

characterisation is underway. Figure 28 shows risetime of signal observed for a setup with bias as shown in figure 26. The target is provided positive bias to collect all electrons and ion channel is provided negative bias to collect the ions in plasma. Figure 28 shows variation in risetime with laser energy. With increase in laser energy, the energy of plasma would also increase, which would result in a lower rise time for ion channel which is located at the top. Whereas, the risetime for target channel will increase with increase in laser energy as electrons would travel further before returning back to target plate. This trend in observed in the figure except for the last point correspoding to 9 mJ. This could be because of multiple laser shots taken at same location on target plate resulting in crater formation and uncertainity in initial direction of kinetic energy of plasma.

## 4. Summary

An impact ionization dust detector is being developed for future planetary missions, to study interplanetary dust particles. Using the detector particle parameters like mass, velocity and flux can be derived. The basic working principle of the detector along with its different components is discussed. The mechanical requirement and design and vibration test and analysis are also mentioned. The analog and processing electronics configuration of the instrument are discussed in detail. Instrument testing in laboratory using simulated pulses are carried out. Simulation for optimizing the instrument performance are carried out using SIMION software and possible damage to detector in space environment is estimated using GEANT4 software. The calibration plan of the instrument with dust accelerator to be carried out in future is mentioned. Further, testing of the instrument with nanosecond pulse laser and derivation of equivalence between a dust particle and pulse laser is shown.

## 5. Acknowledgment

We would like to thank: S. M. K. Praneeth, J. B. Rami and the Structures Division in SAC, Ahmedabad for their help with structure design optimization, analysis and vibration tests. Dr. Rajesh Kumar Singh at IPR, Bhat for his support with pulse laser facility and his guidance.

The editor, D. Pallamraju, thanks Himanshu S. Mazumdar, Ashish Mishra, and Shantanu Karkari for their assistance in the evaluation of this Technical Note.

## References

Altobelli, N. et al. (2006). A new look into the Helios dust experiment data: presence of interstellar dust inside the Earth's orbit. *A&A*, 448(1):243–252.

Austin, D. E. et al. (2002). Dustbuster: a compact impact-ionization time-of-flight mass spectrometer for in situ analysis of cosmic dust. *Review of Scientific Instruments*, 73(1):185–189.

Berg, O. E. and Grün, E. (1973). Evidence of hyperbolic cosmic dust particles. *Space Research*, 13:1047–1055.

Campbell-Brown, M. D. (2008). High resolution radiant distribution and orbits of sporadic radar meteoroids. *Icarus*, 196(1):144–163.

Carrillo-Sánchez et al. (2020). Cosmic dust fluxes in the atmospheres of Earth, Mars, and Venus. *Icarus*, 335:113395.

Carrillo-Sanchez, J. D. et al. (2020). Cosmic dust fluxes in the atmospheres of earth, mars, and venus. *Icarus*, 335:113395.

Crismani, M. M. J. et al. (2017). Detection of a persistent meteoric metal layer in the Martian atmosphere. *Nature Geoscience*, 10(6):401–404.

Dietzel, H. et al. (1972). Micrometeoroid simulation studies on metal target. *Journal of Geophysical Research*, 77:1375–1395.

Drapatz, S. and Michel, K. W. (1974). Theory of Shock-Wave Ionization upon High-Velocity Impact of Micrometeorites. *Zeitschrift für Naturforschung A*, 29a:870–879.

Drolshagen, G. (2008). Impact effects from small size meteoroids and space debris. *Advances in Space Research*, 41(7):1123–1131.

Fletcher, A. et al. (2015). Simulating plasma production from hypervelocity impacts. *Physics of Plasmas*, 22(9):093504.

Frost, V. C. (1970). Meteoroid damage assessment. Technical Report NASA SP-8042, NASA.

Galligan, D. P. and Baggaley, W. J. (2004). The orbital distribution of radar-detected meteoroids of the Solar system dust cloud. *Monthly Notices of the Royal Astronomical Society*, 353(2):422–446.

Göller, J. R. and Grün, E. (1989). Calibration of the galileo/ulysses dust detectors with different projectile materials and at varying impact angles. *Planetary and Space Science*, 37(10):1197–1206.

Grün, E. (1984). Impact ionization from gold, aluminum and pcb-z. In Guyenne, T. D., editor, *ESA Special Publication*, volume 224, pages 39–41.

Grün, E. et al. (1985). Collisional Balance of the Meteoritic Complex. In *Lunar and Planetary Science Conference*, Lunar and Planetary Science Conference, pages 267–268.

Grün, E. et al. (1992a). The Galileo Dust Detector. *Space Science Review*, 60(1-4):317–340.

Grün, E. et al. (1992b). The ULYSSES dust experiment. *Astronomy and Astrophysics Supplement Series*, 92(2):411–423.

Grün, E. et al. (2002). Analysis of Impact Ionization From 300 Km/s Fast Projectiles. In *EGS General Assembly Conference Abstracts*, EGS General Assembly Conference Abstracts, page 1921.

Hirai, T. et al. (2014). Microparticle impact calibration of the Arrayed Large-Area Dust Detectors in INterplanetary space (ALADDIN) onboard the solar power sail demonstrator IKAROS. *Planetary and Space Science*, 100:87–97.

Horányi, M. et al. (2008). The Student Dust Counter on the New Horizons Mission. *Space Science Review*, 140(1-4):387–402.

Horányi, M. et al. (2014). The Lunar Dust Experiment (LDEX) Onboard the Lunar Atmosphere and Dust Environment Explorer (LADEE) Mission. *Space Science Review*, 185(1-4):93–113.

Hunt, S. M. et al. (2004). Determination of the meteoroid velocity distribution at the earth using high-gain radar. *Icarus*, 168(1):34–42.

Igenbergs, E. et al. (1998). Mars Dust Counter. *Earth, Planets and Space*, 50:241–245.

Jyoti, G. et al. (1999). Mass spectrometer calibration of high velocity impact ionization based cosmic dust analyzer. *International Journal of Impact Engineering*, 23(1, Part 1):401–408.

Lee, N. et al. (2013). Theory and experiments characterizing hypervelocity impact plasmas on biased spacecraft materials. *Physics of Plasmas*, 20(3):032901.

Mandeville, J. C. (1991). Study of cosmic dust particles on board LDEF: The FRECOPA experiment. *Advances in Space Research*, 11:101–107.

Pabari, J. P. et al. (2018). Orbital altitude dust at Mars, its implication and a prototype for its detection. *Planetary and Space Science*, 161:68–75.

Pabari, J. P. et al. (2022). IDP detection in Earth environment: Prediction of plasma capture efficiency and detector response to high-energy particles. *Planetary and Space Science*, 215:105452.

Srama, R. et al. (2004). The Cassini Cosmic Dust Analyzer. *Space Science Review*, 114(1-4):465–518.

Sykes, M. V. et al. (2004). The interplanetary dust complex and comets. In Festou Michel C., K. H. U. and A., W. H., editors, *Comets II*, page 677. University of Arizona Press, Tucson.

Tripathi, K. R. et al. (2022). Characteristic features of v0 layer in the venus ionosphere as observed by the akatsuki orbiter: Evidence for its presence during the local noon and post-sunset conditions. *Geophysical Research Letters*, 49(7):e2022GL097824.

Whalley, C. L. and Plane, J. M. C. (2010). Meteoric ion layers in the martian atmosphere. *Faraday Discuss.*, 147:349–368.

Wiegert, P. et al. (2009). A dynamical model of the sporadic meteoroid complex. *Icarus*, 201(1):295–310.

Yano, H. et al. (1996). Microscopic and chemical analyses of major impact sites on timeband capture cell experiment of the eureca spacecraft. *Advances in Space Research*, 17:189–192.

# 6. Appendix A

## 6.1 Noise Computation

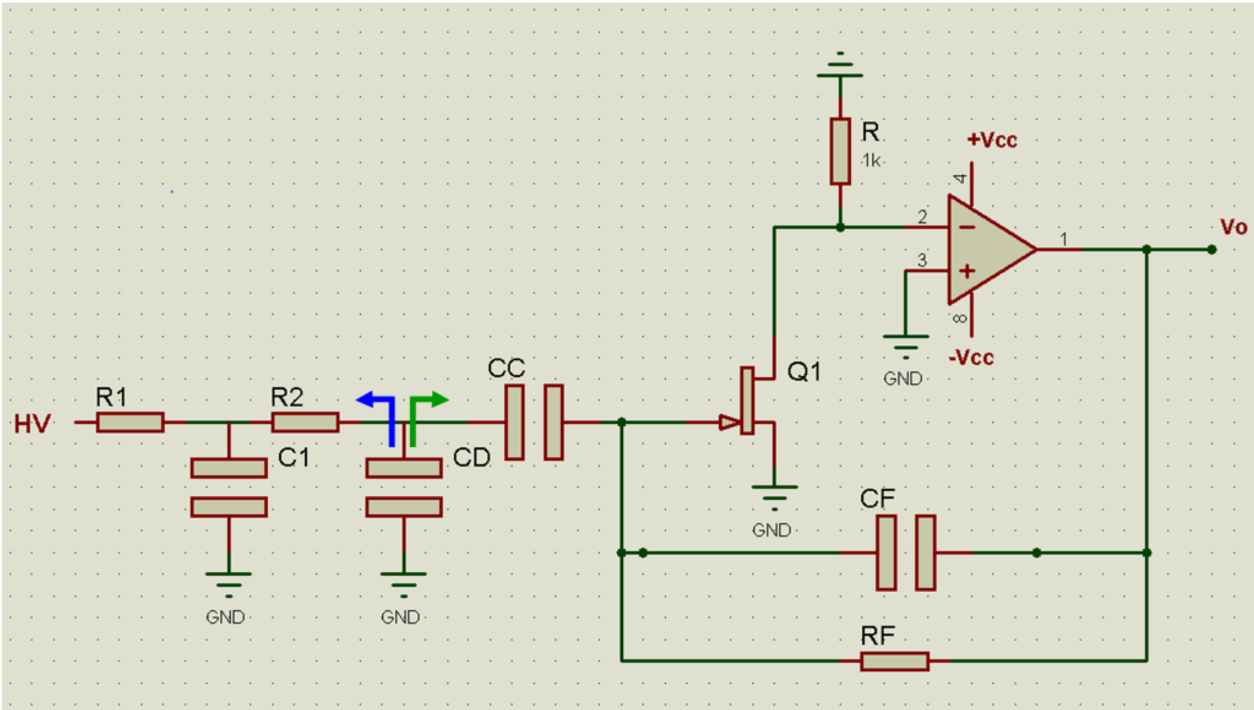


**Figure A1.** Analog circuit with different noise generating sources discussed in the section. The arrow above detector capacitor CD shows the two path for current of which blue colored one is high impedance path and green color shows low impedance path.

### 6.1.1 FET Thermal Noise

The noise is computed using following equation, where $k$ is Boltzmann constant, $g_m$ is transconductance of first stage FET taken as 30 mS and $T$ is absolute temperature. The FET is shown as part Q1 in figure A1.

$$e_{n1} = \sqrt{\frac{8kT}{3g_m}} \tag{17}$$

$$e_{n1} = 6.3 \times 10^{-10} \left( \frac{V}{\sqrt{Hz}} \right) \tag{18}$$

### 6.1.2 Thermal Noise from Feedback Resistor ($R_{f1}$)

The feedback resistor is shown in circuit figure A1, represented by RF. With the factors $A$=20000 and $R_f$ =1 GΩ, the noise is computed using

$$e_{n2} = \sqrt{4kTR_{f1}} \tag{19}$$

where $R_{f1} = \frac{R_f}{1+A}$

$$e_{n2} = 2.98 \times 10^{-8} \left( \frac{V}{\sqrt{Hz}} \right) \tag{20}$$

### 6.1.3 Thermal Noise from HV Bias Resistor ($R_B$)

The resistors in HV bias network are represented as R1 and R2 in figure A1. In the equation, $R_B$=20 MΩ.

$$e_{n2} = \sqrt{4kTR_B} \tag{21}$$

$$e_{n3} = 5.97 \times 10^{-7}\left(\frac{V}{\sqrt{Hz}}\right) \tag{22}$$

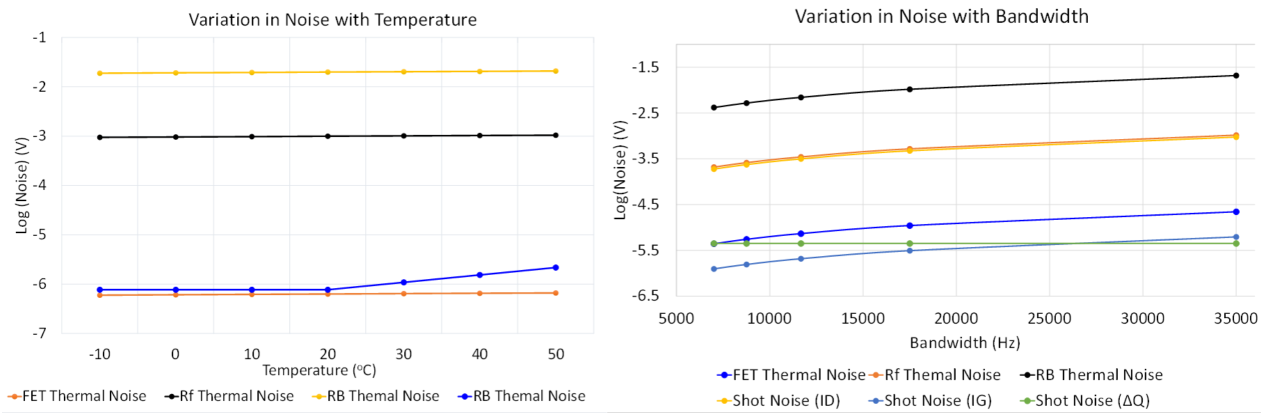


**Figure A2.** Variation in noise from different sources due to Temperature (left) and bandwidth (right). As observed thermal noise from resistors contributes the most.

#### 6.1.4 Shot Noise (FET Gate Leakage)

The leakage current is given by

$$i_n = \sqrt{2qI_G} \tag{23}$$

where gate leakage current $I_G$=1 nA and $C_G$=15 pF.

$$e_{n4} = i_n \times X_{C_g} \tag{24}$$

$$e_{n4} = 2.70 \times 10^{-8}\left(\frac{V}{\sqrt{Hz}}\right) \tag{25}$$

#### 6.1.5 Shot Noise (Detector Leakage)

The leakage current is given by

$$i_{n2} = \sqrt{2qI_D} \tag{26}$$

where detector leakage current $I_D$ = 0.2 pA and for FR4 volume resistivity being $10^6$ to $10^{10}$ MΩ-cm, an average value of $10^8$ MΩ-cm is taken.

$$e_{n5} = 1.78 \times 10^{-10}\left(\frac{V}{\sqrt{Hz}}\right) \tag{27}$$

#### 6.1.6 Shot Noise (Variation in amount of charge)

Taking N as the number of charge carriers,

$$\omega_n^2 = Ne^2 \tag{28}$$

$$e_{n6} = \frac{Ne^2}{C_D} \tag{29}$$

$$e_{n6} = 4.48 \times 10^{-6}(V) \tag{30}$$

The total noise is computed based on input charge range of 5 fC to 0.125 pC corresponding to input signal of 2.5 mV to 250 mV and bandwidth of 35 kHz.

$$V_n = \sqrt{e_{n1}^2 + e_{n2}^2 + e_{n3}^2 + e_{n4}^2 + e_{n5}^2 + e_{n6}^2} = 0.112mV \tag{31}$$

## 7. Appendix B

The two configurations of buffer i.e. inverting for ion channel and non-inverting for electron channel are tested for linearity and the results are shown below. The test was conducted in laboratory with pulse signal provided by a function generator under normal atmospheric conditions. As observed, the output of buffer shows a linear relationship with input as expected.

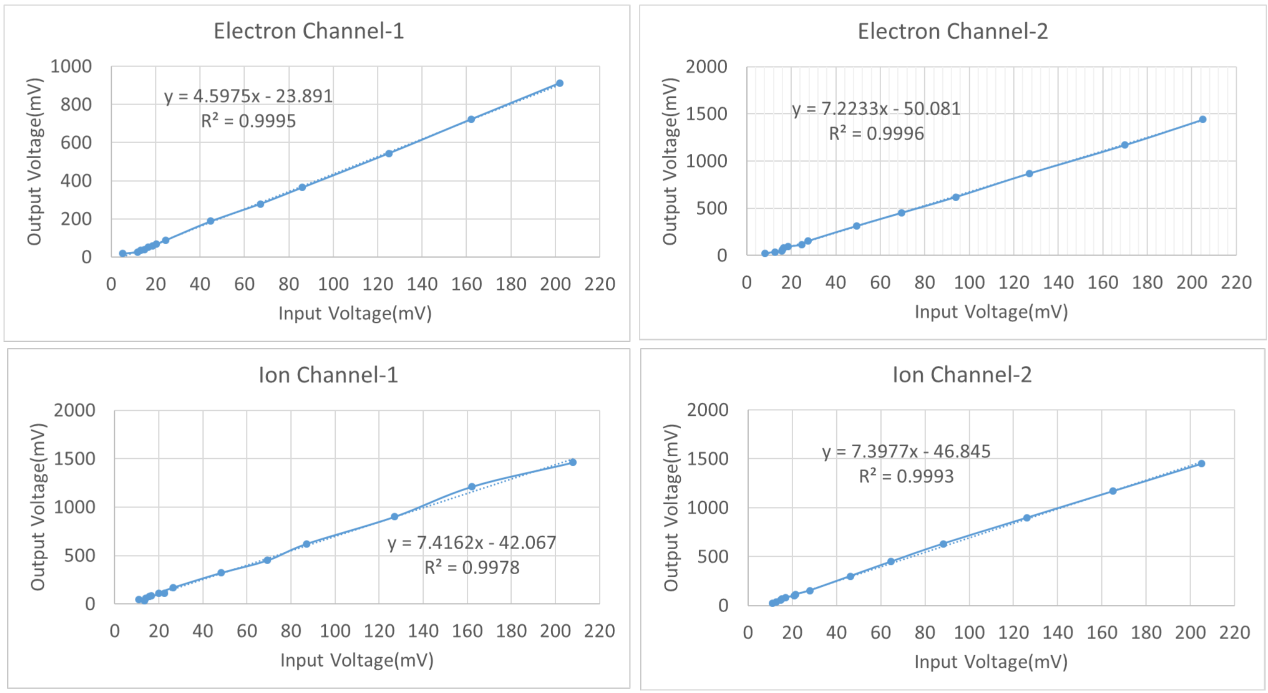


**Figure A3.** Linearity Test of different buffer configurations for all the collecting plates

PRL research
encompasses
the earth
the sun
immersed in the fields
and radiations
reaching from and to
infinity,
all that man's curiosity
and intellect can reveal

पीआरएल के
अनुसंधान क्षेत्र में
समविष्ट हैं
पृथ्वी एवं
सूर्य
जो निमीलित हैं
चुंबकीय क्षेत्र एवं विकिरण में
अनंत से अनंत तक
जिन्हे प्रकट कर सकती है
मानव की जिज्ञासा एवं विचारशक्ति